nature catalysis

Article

https://doi.org/10.1038/s41929-025-01372-z

Steering oxygen-centred radicals with ground-state ene-reductases for enantioselective intermolecular hydroalkoxylations

Received: 11 June 2024

Accepted: 6 June 2025

Published online: 4 July 2025

Check for updates

Bin Chen[1,4], Qiaoyu Zhang[2,4], Jinhai Yu[1,4], Beibei Zhao[1], Ran Ge[1,3], Zihan Zhang[1], Ding Luo[2], Binju Wang[2] ✉ & Xiaoqiang Huang[1] ✉

Enzymes are emerging as promising catalysts for selective radical transformations. However, non-natural radical-type enzymatic catalysis is currently limited to utilizing C-, N- and S-centred radical species. Alkoxy radicals are recognized as versatile intermediates with high reactivity, typically engaging in reactivity modes such as hydrogen atom transfer, β-scission processes and intramolecular addition to alkenes. Enantioselective intermolecular alkoxy radical addition to alkenes remained unknown. Here we develop a biocatalytic strategy based on engineered ene-reductases that facilitate the radical hydroalkoxylation of oxygen-centred radicals with alkenes. A single, ground-state ene-reductase adeptly controls the biocompatible generation of O-radicals, the follow-up intermolecular O-radical addition to alkenes and the final prochiral C-radical termination, achieving high chemo- and enantioselectivity (both enantiomers are obtained separately with different enzymes). Mechanistic experiments, including computational simulations, reveal that the radical enzymatic reaction initiates via a ground-state single-electron transfer and elucidate the origins of enantiodiscrimination of the overall reaction.

Alkoxy radicals are open-shell species that play a crucial role as key reactive chemical intermediates in organic synthesis[1]. These radicals exhibit unique reactivities attributed to the unpaired electron on the highly electrophilic O-atom. The general reactivity modes of alkoxy radicals include intra- or intermolecular hydrogen atom transfer (HAT)[2–4], β-scission processes[5,6] and radical addition onto an unsaturated bond[7,8] (Fig. 1a). While HAT and β-scission processes are well documented to yield more stable carbon-centred radicals, direct utilization of the alkoxy function group through alkoxyl radical addition to alkenes is relatively underexplored[1]. In contrast to N- and S-centred radicals, which are often trapped by C=C bonds, O-radical additions to alkenes typically proceed in intramolecular fashions, leading to O-containing cyclic compounds via kinetically favoured cyclizations. Only a few photocatalytic alkene alkoxy-functionalizations involve the step of alkoxy radical addition to C=C bonds intermolecularly[9,10], such as the work from Dagousset's group[9] on the difunctionalization of alkenes

[1]State Key Laboratory of Coordination Chemistry, Chemistry and Biomedicine Innovation Center (ChemBIC), Frontier Interdisciplinary Science Research Center, School of Chemistry and Chemical Engineering, Nanjing University, Nanjing, China. [2]State Key Laboratory of Physical Chemistry of Solid Surfaces and Fujian Provincial Key Laboratory of Theoretical and Computational Chemistry, College of Chemistry and Chemical Engineering, Xiamen University, Xiamen, China. [3]Department of Chemical and Biochemical Engineering, College of Chemistry and Chemical Engineering, Key Laboratory for Synthetic Biotechnology of Xiamen City, Xiamen University, Xiamen, China. [4]These authors contributed equally: Bin Chen, Qiaoyu Zhang, Jinhai Yu.
✉e-mail: wangbinju2018@xmu.edu.cn; huangx513@nju.edu.cn

https://doi.org/10.1038/s41929-025-01372-z

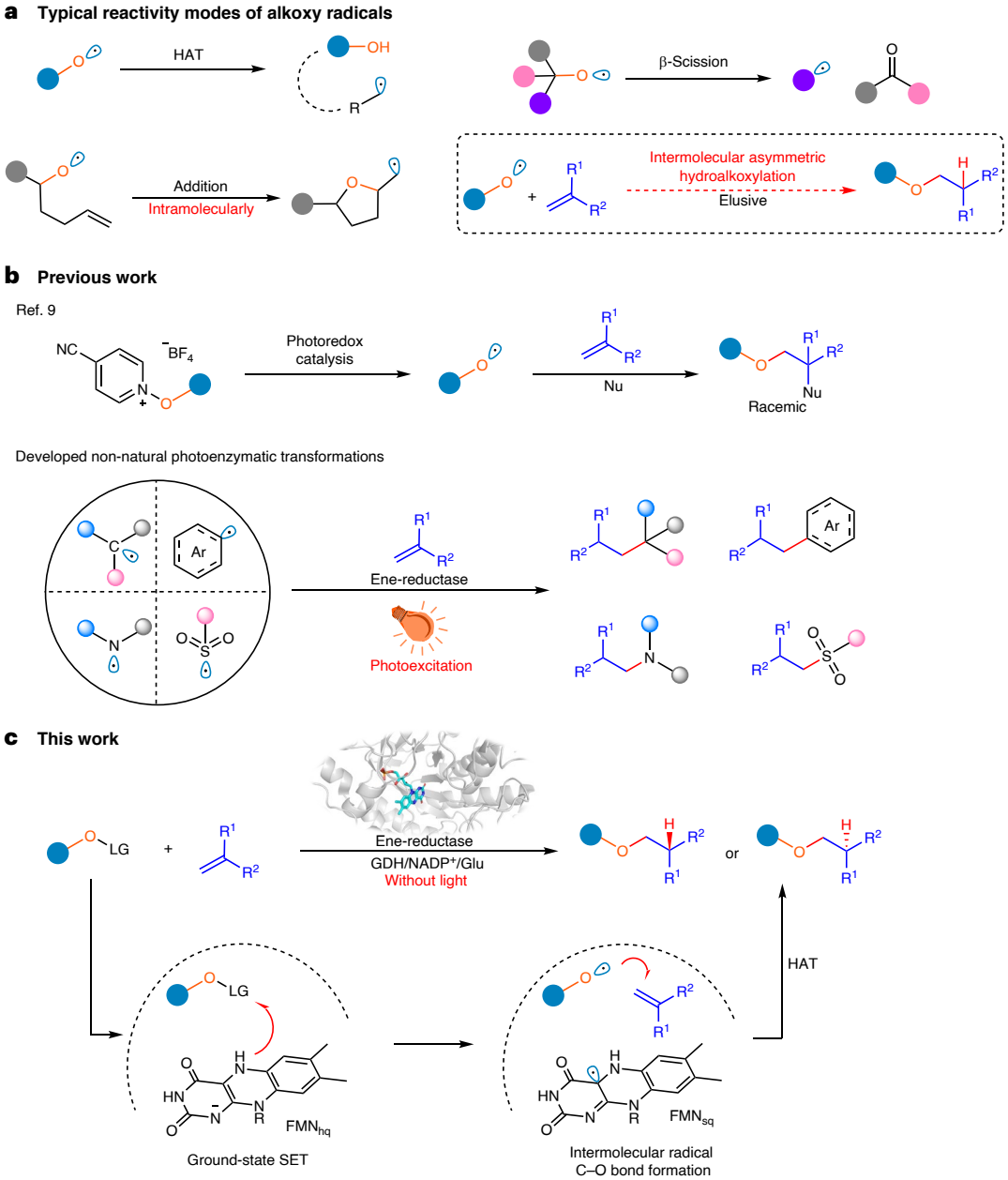

Fig. 1 | ER-enabled enantioselective radical biocatalysis. a, Typical reactivity modes of alkoxy radicals. **b**, Previously reported chemocatalysed O-radical addition to alkenes and photo-induced ER-catalysed non-natural transformations[9]. **c**, This work: an intermolecular O-radical addition to alkenes enabled by ground-state ERs. Nu, nucleophiles including water, alcohol and acetonitrile; Glu, glucose; $FMN_{hq/sq}$, flavin mononucleotide with hydroquinone/semiquinone form; LG, leaving group. The dot curvature indicates the chiral enzyme active site.

using alkoxyl radicals derived from *N*-alkoxypyridinium salts. To the best of our knowledge, asymmetric intermolecular radical hydroalkoxylation has yet to be achieved[11,12], although a non-asymmetric version has recently been reported by Zuo and co-workers during the revision of this work[13].

Recently, notable strides have been made in catalysing non-natural radical biotransformations[14–19]. In particular, the combination of ene-reductases (ERs)[20–22] and visible light catalysis[23], the latter of which has been proven to be a potent tool for generating diverse radical species[24], promotes the development of non-natural photoenzymatic transformations[25,26]. However, the spectrum of radical species manipulated in this arena is confined primarily to carbon-, nitrogen- and sulfur-centred radicals (Fig. 1b). Notable contributions include those of Hyster[27,28], Zhao[29,30], Xu[31] and Rao[32] et al., who have used ERs for the addition of various C-centred radicals to alkenes. Typically, photoexcitation of an ER-associated electron donor–acceptor complex[33] initiates the C-radical species generation. More recently, our group has repurposed ERs by direct visible-light excitation of flavin cofactor to trigger the formation of aryl radical[34] and alkene radical cation species[35]. In addition to C-radical-mediated reactions, Hyster[36], Zhao[37,38] and our group[39] have independently used illuminated ERs to control N-centred radical species, providing elegant examples of enzymatic radical hydroaminations with C=C bonds. In addition, photoenzymatic sulfonyl radical additions to alkenes using ERs have been developed by Xu[40,41] and Ye[42] groups.

However, the alkoxy radical has yet not been harnessed for selective biotransformation. The challenges stem not only from the inherently disfavoured intermolecular addition of alkoxy radical to alkenes[1]

https://doi.org/10.1038/s41929-025-01372-z

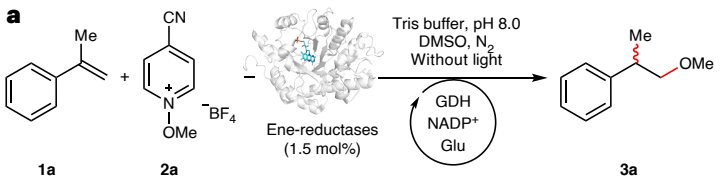

Entry	ER	Deviation from the above conditions[a]	Yield (%)[b]	e.r. (*S*:*R*)[c]
1	YersER	None	73	2:98
2	CsER	None	63	8.5:91.5
3	MorB	None	57	65:35
4	GluER	None	43	85:15
5	GluER-H128Y-Q232L	None	76	92:8
6	YersER	W/o GDH/NADP$^+$/Glu	0	n.a.
7	None	5 mol% FMN added	0	n.a.
8	YersER	Air instead of N_2	47	2:98
9	GluER-H128Y-Q232L	0.5 mol% loading	64	92:8

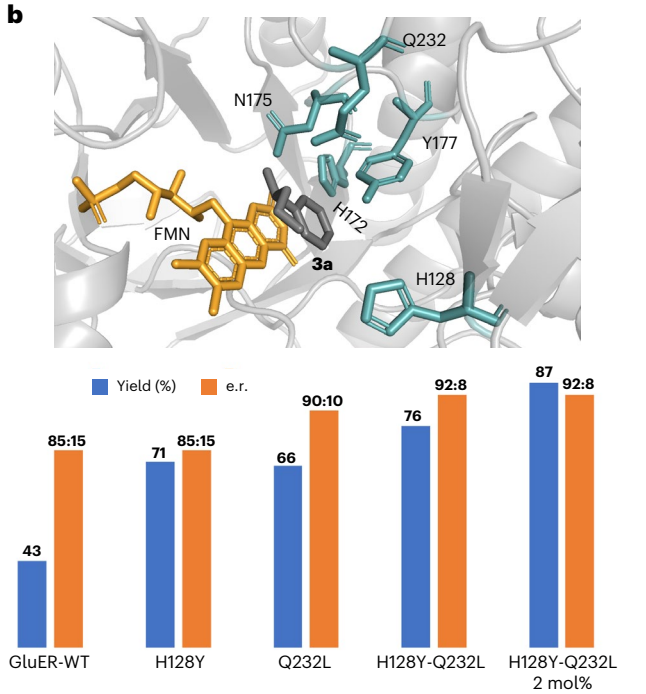

Fig. 2 | Reaction development. a, The effect of ERs and control reactions. [a]Conditions: α-methyl styrene **1a** (0.004 mmol), pyridinium salt **2a** (0.02 mmol), ER (1.5 mol%), GDH (4 U ml^{-1}), NADP$^+$ (5 mol%), glucose (0.02 mmol) and 10% v/v DMSO in Tris buffer (50 mM, pH 8.0) were stirred for 12 h at room temperature under a N_2 atmosphere; total volume of the reaction is 1.0 ml. [b]Yield was determined by GC; [c]e.r. was determined by HPLC analysis on a chiral stationary phase. n.a., not applicable. The absolute configuration of **3a** obtained was assigned by the comparison of retention time on HPLC with the enantiopure standard (*S*)-**3a** (see 'Stereochemistry Assignments' in the Supplementary Methods). **b**, Engineering of GluER for (*S*)-**3a** (see Supplementary Table 9 for docking details).

but also from the absence of a general and effective method for introducing alkoxy radicals and directing the subsequent reactions under enzymatic conditions. Motivated by our ongoing interests in redesigning enzymes for non-natural radical biocatalysis[43–45], we questioned how to develop a biocatalytic strategy that could guide alkoxyl radicals for the challenging intermolecular O-radical addition to alkenes.

Here, we present our latest development concerning ER-catalysed intermolecular radical hydroalkoxylation of alkenes via a ground-state single-electron transfer (SET) pathway (Fig. 1c). Alkoxy radicals are harnessed to unlock enzyme reactivity that are inaccessible through traditional chemocatalysis. The mechanistic aspects of this reaction include the following: the alkoxy radical species are selectively generated through ground-state SET initiated by the flavin hydroquinone cofactor (FMN_{hq}); within the confined active site, alkoxy radicals selectively add to the C=C bond intermolecularly, leading to the formation of a stabilized prochiral benzylic C-radical; and stereoselective HAT directed by two classes of ER gives enantiodivergent synthesis of ethers (up to 99.5:0.5 enantiomeric ratio, e.r.).

Results

Reaction development

To develop the envisioned non-natural enzymatic radical C–O formation, α-methyl styrene **1a** was chosen as the radical acceptor, and *N*-alkoxypyridinium salt **2a** was selected as a potential source of methoxy radical. Given the redox potential of **2a** (E_{red} (**2a**) = −0.47 V versus saturated calomel electrode (SCE)[46], we envisioned that ground-state ERs with the reduced form flavin cofactor FMN_{hq} (redox potential −0.45 V versus SCE)[47] could reduce **2a** without the need for light illumination[48,49]. The natural turnover system of ERs, containing nicotinamide adenine dinucleotide phosphate (NADP$^+$), glucose dehydrogenase (GDH) and glucose, was used to regenerate FMN_{hq}. After testing a batch of ERs heterologously overexpressed in our laboratory, we found that an ER isolated from *Yersinia bercovieri* (YersER) displayed the highest efficiency and enantioselectivity, giving **3a** in 73% yield with (*R*)-preferred selectivity (2:98 e.r.; Fig. 2a, entry 1). By contrast, *Gluconobacter* ER (GluER) delivered product **3a** in 43% yield with (*S*)-preferred selectivity (85:15 e.r.; Fig. 2a, entry 4).

To further improve the yield and enantioselectivity for (*S*)-**3a**, semi-rational site-specific engineering[50,51] was conducted on the basis of the docking profile of (*S*)-**3a** and the modelled GluER protein structure (PDB 6O08) (Fig. 2b). Five amino acid residues (H128, H172, N175, Y177 and Q232) were chosen for site-specific mutagenesis (Supplementary Table 6), resulting in two beneficial single-site mutants: GluER-H128Y, which increased yield to 71% (85:15 e.r.), and GluER-Q232L, which noticeably improved enantioselectivity and yield (90:10 e.r., in 66% yield). The combination of these two single-site mutants generated a new variant GluER-H128Y-Q232L, delivering (*S*)-**3a** in 76% yield, with a 92:8 e.r. (Fig. 2a, entry 5). Furthermore, by applying the enzyme loading to 2 mol%, (*S*)-**3a** was obtained in 87% yield, without affecting enantioselectivity (Fig. 2b).

Control experiments using riboflavin 5-monophosphate sodium salt (flavin mononucleotide, FMN) instead of ER or in the absence of the NADPH regeneration system confirmed that both enzyme and reductant are required for the reactivity, as no product **3a** was formed (Fig. 2a, entries 6 and 7). In the presence of air, the yield notably decreased, but the enantioselectivity remained high (Fig. 2a, entry 8). Notably, lowering the enzyme loading to 0.5 mol% resulted in a turnover number of 128 (Fig. 2a, entry 9).

Substrate scope

Next, we assessed the substrate scope of the non-natural radical hydroalkoxylation (Fig. 3 and Supplementary Figs. 3 and 4). A small selection of ERs were screened for the substrates showing poor enantioselectivity with the standard variants. YersER (ER1), *Caulobacter segnis* ER

https://doi.org/10.1038/s41929-025-01372-z

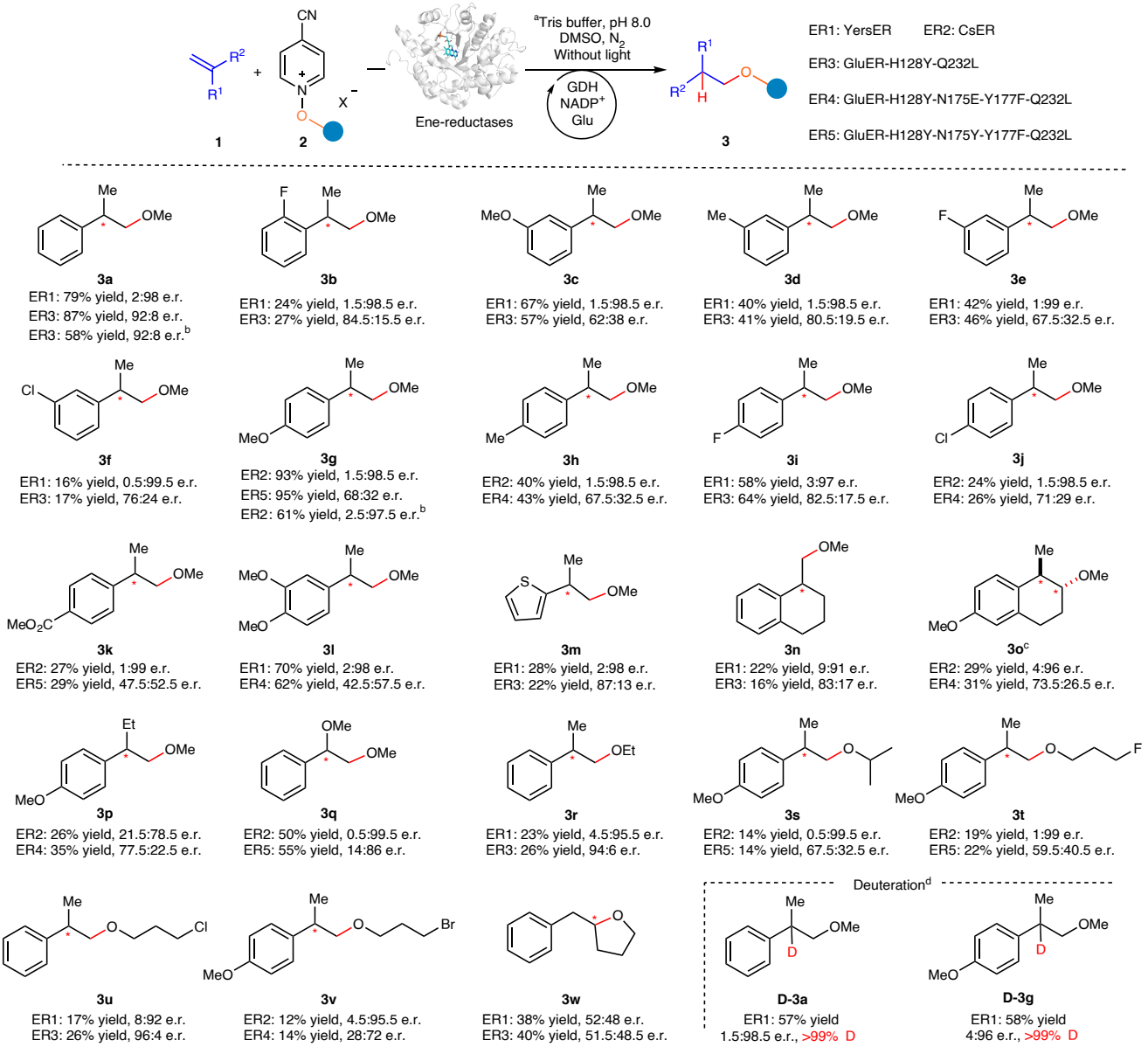

Fig. 3 | Scope investigation. [a]Standard conditions: alkene **1** (0.008 mmol, 1 equiv.), pyridinium salt **2** (0.04 mmol, 5 equiv.), ER (2 mol%), GDH (4 U ml^{-1}), NADP$^+$ (5 mol%), glucose (0.04 mmol, 5 equiv.) and 10% v/v DMSO in Tris buffer (50 mM, pH 8.0) were stirred for 12 h at room temperature under a N_2 atmosphere; the total volume of the reaction is 2.0 ml. [b]Isolated yield based on a 0.1 mmol reaction; the loading of enzyme is 1 mol%. [c]**3o** d.r. >20:1. [d]NADP$^+$ (1 mol%), deuterated glucose (0.02 mmol, 2.5 equiv.) and deuterated Tris buffer were used, and percentages of deuterium incorporation were determined by ^{1}H NMR analysis. X = BF_4 for **3a**–**r**, X = OTf for **3s**–**w**; these pyridinium salts are synthesized by different methods, resulting in different counter anions[9]. Duplicated runs using different batches of enzyme yielded results within ±5% error in yield and within ±2% error in enantiomeric excess. D, deuterium.

(CsER, ER2), GluER-H128Y-Q232L (ER3), GluER-H128Y-N175E-Y177F-Q232L (ER4) or GluER-H128Y-N175Y-Y177F-Q232L (ER5) were used to produce both enantiomers of the products. Using *N*-alkoxypyridinium salt **2a** as the radical precursor, a range of substituted methyl styrenes underwent enantiodivergent hydroalkoxylation smoothly. These substrates included different substituents positioned *para*, *meta* or *ortho* to the phenyl group (**3a**–**k**), disubstitutions (**3l**) and a thienyl group (**3m**), all of which were well tolerated. The yields varied, and a styrene with a highly electron-deficient group (**3k**) exhibited decreased yields. Tetrahydronaphthalene-derived alkenes (**3n** and **3o**) performed well, especially for **3o** bearing two stereocentres (up to a 4:96 e.r. with >20:1 diastereomeric ratio). Variations at the α-position of alkene also affect reaction outcomes (**3p** and **3q**). For instance, vinyl ether **1q** was effective, generating 1,2-diether **3q** with good enantioselectivity, although only one enantiomer was obtained with the ERs tested. Furthermore, several alkoxy radical precursors were evaluated, and **3r**–**v** were successfully constructed enabled by the present catalysis. Despite the relatively low yields, the enantioselectivity reached up to 0.5:99.5 e.r. An intramolecular radical hydroalkoxylation was also tested, resulting in moderate yield and poor stereoselectivity (**3w**), suggesting challenges in controlling the initial C–O bond formation. The reaction is easily scaled up while maintaining equivalent enantioselectivity (**3a** and **3g**) with a reduced ERs loading of 1 mol%. From the perspective of yield, electron-rich substituents on the *para* position of styrenes appeared beneficial (**3g** versus **3j**), which could be ascribed to the electronic philicity preference of O-radicals. Furthermore, we investigated the effect of substituents on the reaction rate. By combining the calculations (Supplementary Figs. 16–18) and kinetics studies (Supplementary Table 8), we found complexity in the factors that influence reaction yields or initial rates (for detailed information, please see 'Analysis of Substrate Specificity' in the Supplementary Information).

https://doi.org/10.1038/s41929-025-01372-z

Biocatalytic deuteration is a far less explored area, but it holds important potential for deuterating unconventional remote sites. For example, the β-position of an ether oxygen atom without requiring additional functionalities is difficult to achieve by chemocatalysis. Based on this developed biocatalytic radical intermolecular hydroalkoxylation, enantioenhanced β-deuterated ethers can be accessed using D-glucose-d1 as the deuteration source, as demonstrated by the synthesis of D-**3a**, and D-**3g**, achieving >99% deuterium incorporation rate at the benzylic position.

Mechanistic studies

A catalytic scheme was proposed (Fig. 4). Initially, GDH-mediated hydride transfer formed the reduced hydroquinone state ER (Int. A → Int. B). SET reduction of radical precursor **2** by the FMN_{hq} generated O-centred radical and semiquinone flavoprotein (Int. C). Subsequently, intermolecular O-radical addition to alkene **1** gave prochiral C-centred radical (Int. D). Then, enzyme-directed HAT furnished enantioenriched product **3** (Int. E). Finally, the release of the product completed the cycle. To verify this scheme, both computational studies and wet experiments were conducted.

First, quantum mechanics (QM) model calculations showed that SET from FMN_{hq} to **2a** had an energy barrier of ~0.1 kcal mol^{-1} (Supplementary Table 16) and an exothermicity of 21.7 kcal mol^{-1} (Fig. 5a), supporting that single-electron reduction for radical initiation was thermodynamically and kinetically favourable at the ground state. This result was consistent with our experiments that additional light illumination was not required for the overall reaction efficiency (Fig. 2a and Supplementary Tables 2 and 3). In addition, the time–curve analysis indicated that the reaction within 5 min was slightly promoted by light irradiation. However, the O-radical progress was so fast that, after 5 min, the reaction without illumination showed no obvious difference in yield compared with that under irradiated conditions (Supplementary Table 3).

Starting from **2a** radicals (**2a·**), quantum mechanics/molecular mechanics (QM/MM) calculations showcased that the cleavage N–O bond process involves an energy barrier of 5.9 kcal mol^{-1} and exothermicity of 4.8 kcal mol^{-1}, leading to the methoxy radical (·OMe) (Fig. 5b and Supplementary Fig. 27). Following methoxy radical formation, we hypothesized that the hydrophilic isonicotinonitrile could diffuse out of the enzyme's active site, allowing its binding site to be occupied by the hydrophobic **1a**. To confirm the presence of this O-radical, we conducted radical trapping experiments with 1,1-diphenylethylene (Fig. 5c). The observation of the methoxy radical adduct supported the generation of methoxy radical intermediate (Fig. 4, Int. C).

To investigate the follow-up O-radical addition (Int. C → Int. D), a radical clock experiment using α-cyclopropyl-styrene **5** was performed (Fig. 5d). Ring-opened product **6** was identified in reactions catalysed by ERs, while in the reaction with FMN alone the product **6** was not observed. These findings supported the presence of an enzymatic benzylic radical intermediate Int. D.

To explore the origin of the different selectivity catalysed by different ERs, the classical molecular dynamics (MD) simulations and QM/MM MD simulations were performed to obtain the more reliable structure of Int. C. Then, QM/MM calculations were conducted to explore the subsequent possible mechanism of alkoxy radical addition pathways. Simulations suggested that **1a** can adopt two possible conformations (CH_3-left and CH_3-right) within the active site of ER3, which ultimately led to *S* and *R* configurations, respectively. Starting from the CH_3-left conformation, the following C–O radical bond formation affording the prochiral radical (Int. D) was a barrierless process (Int. C → Int. D; Fig. 5f). In addition, we investigated the undesired side pathway that forms methanol via HAT from FMN_{sq} to methoxy radical (Int. C → TS3), which involved an energy barrier of 3.7 kcal mol^{-1}, indicating that methoxy radical preferred the addition to the C=C bond (Fig. 5f).

To gain further insights into the radical termination of Int. D, isotopic labelling experiments were conducted (Fig. 5e). When the reaction

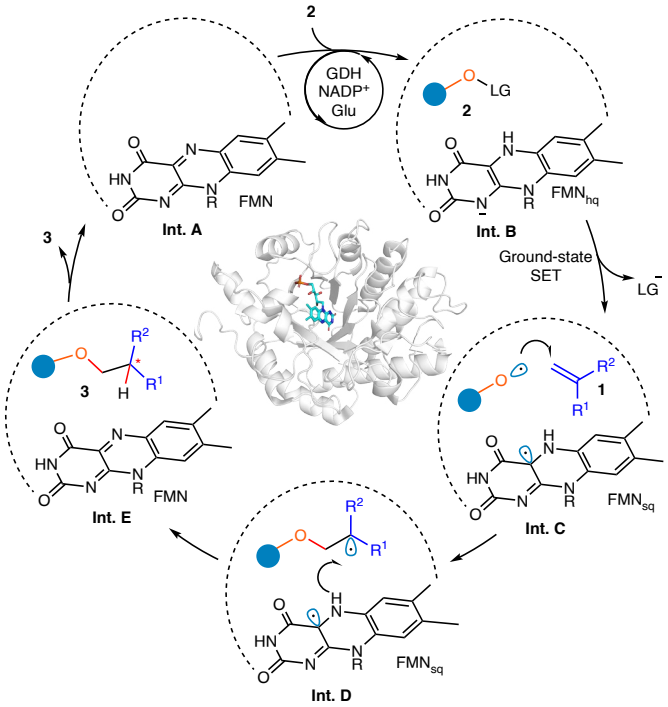

Fig. 4 | Proposed catalytic cycle under dark conditions. Glu, glucose; LG, leaving group; FMN_{hq}, hydroquinone form of FMN; FMN_{sq}, semiquinone form of FMN.

was conducted with D-glucose-d1 where deuterated $FMND^-$ formed in situ, the newly formed stereogenic centre was labelled with 82% deuterium, and only 11% deuterium was incorporated when deuterated buffer was applied. These implied that the H-atom abstracted by the benzylic radical was mediated by FMN_{sq} (Int. D → Int. E). Our QM/MM-calculated energy profiles of alkoxy radical addition pathways further supported the key FMN_{sq}-mediated HAT step. As shown in Fig. 5f, HAT from FMN_{sq} to the Int. D (CH_3-left) generated the product **3a** in *S*-configuration with a barrier of 10 kcal mol^{-1} (Int. D → TS2_*S*), while generating *R*-configuration required a barrier of 14.3 kcal mol^{-1} (Int. D → TS2_*R*). The QM/MM results suggested that the HAT process was the rate-determining step, aligning with our kinetic isotope effect (KIE) experimental results (k_H/k_D = 4.3; see 'KIE Experiment' in the Supplementary Methods). In addition, the QM/MM-calculated KIE (calculated from k_H'/k_D'; Supplementary Fig. 32) was 4.3, which is consistent with the experimental values, thereby confirming the reliability of our calculations.

As shown in Fig. 5f, the corresponding C–O coupling involved a barrier of 2.6 kcal mol^{-1} (Int. C → TS1_*R*), which was 2.6 kcal mol^{-1} higher than that of the CH_3-left conformation (barrierless process for Int. C → TS1_*S*). This was mainly because the methoxy radical was further away from the double bond of **1a** in the CH_3-right conformation (Fig. 5f). In addition, analysis of the structure of TS1_*R* revealed that the C–O coupling process involved repulsion between the CH_3 substituent of **1a** and FMN_{sq}, potentially increasing the energy barrier (Supplementary Fig. 34). As the C–O coupling step was highly exothermic and irreversible, it was clear that the enantioselectivity would be controlled by the C–O coupling rather than the subsequent HAT step. Although the HAT step in the active site constructed the stereocentre, the binding conformational selection of the α-methyl styrene substrate determined the configurations of the prochiral carbon-centred radical, which subsequently determined the absolute configuration of the newly formed stereocentre. Owing to the substrate positioning in the active site of ER3, the generation of (*S*)-**3a** was kinetically preferred, which well explained the experimental outcome that ER3 gave the formation of (*S*)-**3a** dominantly (Fig. 2a).

https://doi.org/10.1038/s41929-025-01372-z

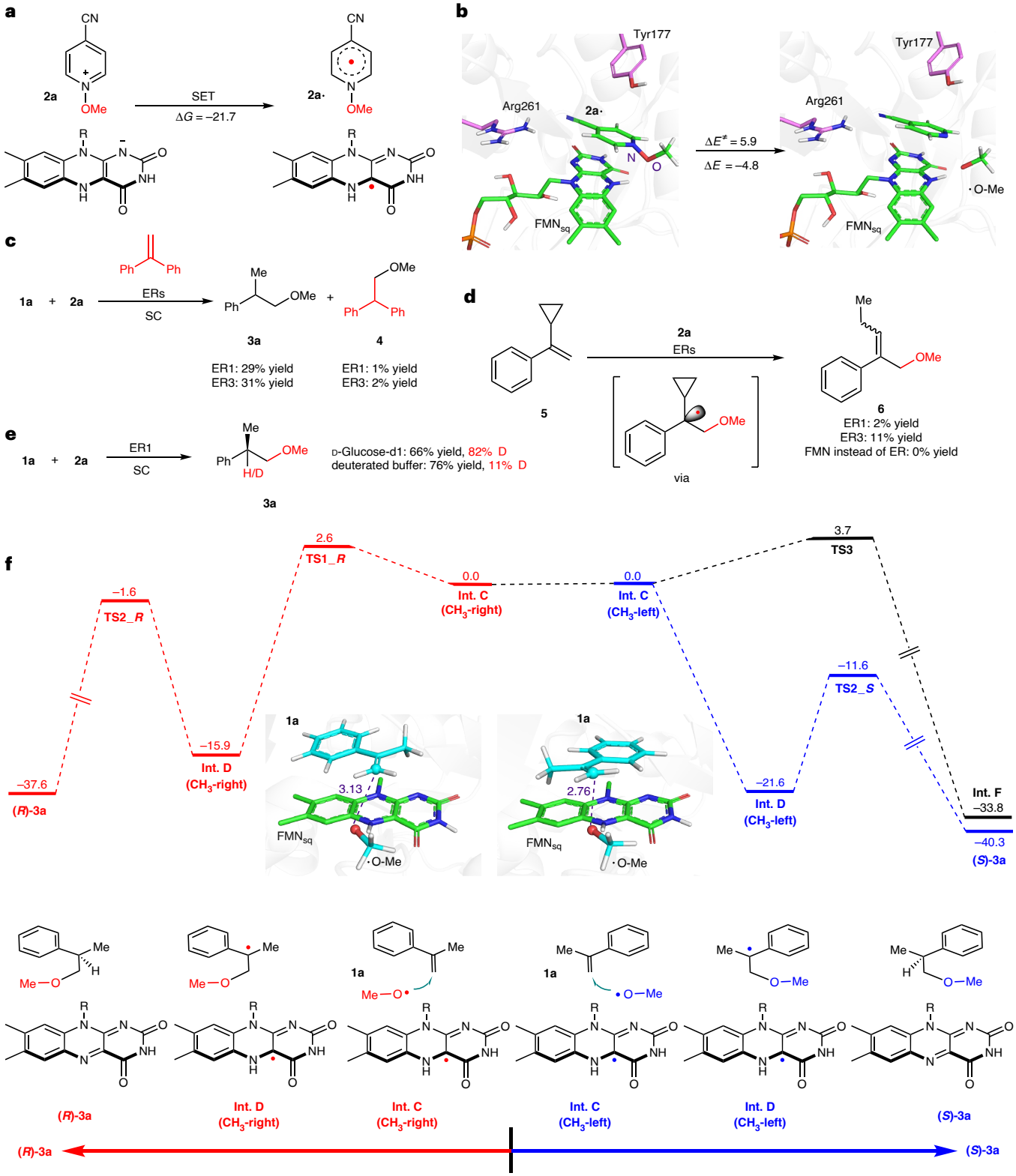

Fig. 5 | Mechanistic studies. a, QM-calculated exothermicity of SET from FMN_{hq} to **2a**. **b**, QM/MM-calculated energy of N–O bond cleavage in **2a·** to form the methoxy radical. **c**, Radical trap experiment. **d**, Radical clock experiment. **e**, Isotope labelling experiment. **f**, QM/MM-calculated energy profiles of ER3-catalysed alkoxy radical addition pathways generating either (*S*)- or (*R*)-**3a** in CH_3-left and CH_3-right conformations, respectively. The unit of energy is given in kcal mol^{-1}; ΔG, the Gibbs free energy change; ΔE, the reaction energy; $\Delta E^{\neq}$, the calculated energy barrier; SC, standard conditions as shown in the legend of Fig. 3.

As for the process catalysed by ER1, further simulations showed that the methoxy radical was in closer proximity to the double bond of **1a** in the CH_3-right conformation than in the CH_3-left conformation. As such, the C–O coupling from the CH_3-right conformation was kinetically favoured to generate (*R*)-**3a** theoretically (Supplementary Figs. 12–15), which aligned with the observed (*R*)-**3a** selectivity with ER1.

For the reaction catalysed by ER3, the calculated C–O coupling barrier for the *S*-configuration was 2.6 kcal mol^{-1} lower than that of

the *R*-configuration, which is close to the energy gap of 1.4 kcal mol^{-1} derived from the experimentally measured e.r. of 92:8 for *S*:*R* (see 'Enantiomeric Excess Calculations' in the Supplementary Methods). Furthermore, with ER1, the calculated energy barrier for the *R*-configuration was 4.6 kcal mol^{-1} lower than that of the *S*-configuration, which matched the experimental 98:2 for the *R*:*S* e.r. value (2.3 kcal mol^{-1} according to the Boltzmann distribution).

Conclusions

We have successfully introduced a ground-state SET mechanism to biocatalysis, enabling the taming of reactive O-centred radicals for a challenging intermolecular hydroalkoxylation. First, we expand the radical spectrum in non-natural radical-type enzymatic catalysis to include O-centred radical species, facilitating the enantiodivergent synthesis of enantioenriched O-containing compounds. Second, we achieve stereocontrolled O-radical-mediated intermolecular hydroalkoxylation. Our mechanistic studies suggest that the exquisite but evolvable enzyme active site triggers the formations of highly reactive alkoxy radical and guides the following intermolecular addition to C=C bond with high efficiency and selectivity. Third, the introduction of an unusual ground-state radical initiation pathway that does not require light illumination complements photoenzymatic catalysis. We anticipate that the herein-reported ground-state SET radical enzyme will inspire the exploration of non-natural asymmetric biotransformations that are challenging for chemocatalysis.

Methods

General procedure for the enzymatic radical hydroalkoxylation

All the biocatalytic reactions were assembled in a glove box with a O_2 concentration below 5 ppm. Here, we use **1a** + **2a** → **3a** as an example. To a 4-ml glass vial with a magnetic stir bar, $NADP^+$ (80 µl, 5 mM stock in Tris buffer, 5 mol%), glucose (80 µl, 500 mM stock in Tris buffer, 0.04 mmol, 5 equiv.), solutions of ER (2 mol%), GDH (1,000 U ml^{-1}, 8 U), substrate **1a** (100 µl, 80 mM **1a** in dimethyl sulfoxide (DMSO), 0.008 mmol, 1 equiv.) and substrate **2a** (100 µl, 400 mM **2a** in DMSO, 0.04 mmol, 5 equiv.) were added to Tris buffer (50 mM, pH 8.0). The reaction mixture was adjusted to a final volume of 2 ml. The reaction vial was sealed with a screw cap, transferred out of the glove box and stirred at ambient temperature for 12 h.

Yields determined by GC

Ethyl acetate (2.0 ml) and 20 µl of an internal standard solution (4% v/v *n*-dodecane in ethyl acetate) were added to the reaction mixture and homogenized. The organic phase was separated and analysed by gas chromatography (GC) and GC–mass spectrometry. The solvent was subsequently evaporated under reduced pressure (caution: the boiling point of the products is low), and the residue was redissolved in hexane for chiral high-performance liquid chromatography (HPLC) analysis.

Yields determined by liquid chromatography

Acetonitrile (2.0 ml) and 200 µl of an internal standard solution (3 mg 1,3,5-tribromobenzene in 1 ml acetonitrile) were added to the reaction mixture and vigorously mixed. The mixture was centrifuged, and the supernatant was filtered and subjected to liquid chromatography analysis.

System set-up and MD simulations

The initial model of GluER-H128Y-Q232L (ER3) was derived from the crystal structure (PDB 6O08) by introducing two mutations, H128Y and Q232L. The structure of YersER (ER1) was prepared using AlphaFold2[52]. Subsequently, **2a** and **1a** were docked into the active site using AutoDock Vina tool[53]. The Amber ff14SB force field[54] was applied to the protein residues, whereas the general AMBER GAFF force field[55] was assigned to **1a**, **2a**, methoxy radical and FMN. The partial atomic charges of **1a**, **2a**, methoxy radical and FMN were derived via restrained electrostatic potential calculations at the B3LYP[56]/6-31G(d,p) level of theory. Sodium ions were introduced to neutralize the overall charge of the system. The final system was solvated in a TIP3P[57] waters extending up to a minimum distance of 16 Å from the protein surface. After appropriate system preparation, full energy minimization, annealing and equilibration were performed. Finally, 100-ns MD simulations were conducted under constant pressure and constant temperature conditions for the FMN, **2a** complex and **1a**, FMN and methoxy radical complex. All simulations were carried out using the graphics processing unit-accelerated version of the AMBER 18 package[58].

It is noteworthy that the SET process from FMN_{hq} to **2a** was calculated using the QM model, where FMN_{hq}, **2a**, FMN_{sq} and **2a** radicals were treated as independent species. All structure optimizations were carried out at the B3LYP-D3/def2-SVP level (labelled B1). Energies were subsequently refined using the larger basis set, def2-TZVP (denoted as B2), for all atoms. Furthermore, QM/MM (B3LYP-D3/B2) calculated the cleavage of the N–O bond of **2a** radicals and alkoxy radical addition to **1a**. In QM/MM calculations, all transition states were located via the highest-energy points along the reaction coordinates on the potential energy surface, followed by full transition state optimization using the dimer method.

QM/MM calculations for enzymatic reactions

A representative snapshot from the QM/MM MD trajectory was selected for subsequent QM/MM calculations. All QM/MM calculations were performed using ChemShell[59,60], which integrates Turbomole[61] for the QM region and DL_POLY[62,63] for the MM region. The electronic embedding scheme[64] was used to account for the polarizing effect of the enzymatic environment on the QM region. The QM/MM boundary was treated using hydrogen link atoms within the charge-shift model. Grimme's D3BJ empirical dispersion[65,66] was included in all calculations. Finally, the QM/MM energies comprised the electronic energies at the B3LYP-D3/B2 level, zero-point energy corrections at the B3LYP-D3/B1 level and Grimme's D3BJ dispersion terms.

Reporting summary

Further information on research design is available in the Nature Portfolio Reporting Summary linked to this article.

Data availability

HPLC spectra and NMR spectra are available in the Supplementary Information. The PDB code of the GluER used in this work is 6O08. The structural data (including all QM calculation coordinates, QM region coordinates from QM/MM calculations and the initial and final configurations of molecular dynamics trajectories) are available via Zenodo at https://doi.org/10.5281/zenodo.14851048 (ref. 67).

Code availability

The codes for building the QSAR model are available via GitHub at https://github.com/ld139/QSAR_enz.

References

1. Chang, L., An, Q., Duan, L., Feng, K. & Zuo, Z. Alkoxy radicals see the light: new paradigms of photochemical synthesis. *Chem. Rev.* **122**, 2429–2486 (2022).
2. Wang, C., Harms, K. & Meggers, E. Catalytic asymmetric C–H functionalization under photoredox conditions by radical translocation and stereocontrolled alkene addition. *Angew. Chem. Int. Ed.* **55**, 13495–13498 (2016).
3. Zhang, J., Li, Y., Zhang, F., Hu, C. & Chen, Y. Generation of alkoxyl radicals by photoredox catalysis enables selective C(sp^3)–H functionalization under mild reaction conditions. *Angew. Chem. Int. Ed.* **55**, 1872–1875 (2016).

4. Hu, A., Guo, J.-J., Pan, H. & Zuo, Z. Selective functionalization of methane, ethane, and higher alkanes by cerium photocatalysis. *Science* **361**, 668–672 (2018).
5. Vasilopoulos, A., Krska, S. W. & Stahl, S. S. C(sp^3)–H methylation enabled by peroxide photosensitization and Ni-mediated radical coupling. *Science* **372**, 398–403 (2021).
6. Yayla, H. G., Wang, H., Tarantino, K. T., Orbe, H. S. & Knowles, R. R. Catalytic ring-opening of cyclic alcohols enabled by PCET activation of strong O–H bonds. *J. Am. Chem. Soc.* **138**, 10794–10797 (2016).
7. Hartung, J., Stowasser, R., Vitt, D. & Bringmann, G. 5-*exo* or 6-*endo*? Exploring transition state structures in cyclizations of 4-penten-1-oxyl radicals. *Angew. Chem. Int. Ed. Engl.* **35**, 2820–2823 (1996).
8. Tsui, E., Metrano, A. J., Tsuchiya, Y. & Knowles, R. R. Catalytic hydroetherification of unactivated alkenes enabled by proton-coupled electron transfer. *Angew. Chem. Int. Ed.* **59**, 11845–11849 (2020).
9. Barthelemy, A. L., Tuccio, B., Magnier, E. & Dagousset, G. Alkoxyl radicals generated under photoredox catalysis: a strategy for anti-Markovnikov alkoxylation reactions. *Angew. Chem. Int. Ed.* **57**, 13790–13794 (2018).
10. Yuan, F. et al. Photoredox-catalyzed multicomponent cyclization of 2-vinyl phenols, *N*-alkoxypyridinium salts, and sulfur ylides for synthesis of dihydrobenzofurans. *ChemCatChem* **13**, 543–547 (2021).
11. Capaldo, L. & Ravelli, D. Alkoxy radicals generation: facile photocatalytic reduction of *N*-alkoxyazinium or azolium salts. *Chem. Commun.* **55**, 3029–3032 (2019).
12. Ali, M., Sewell, S., Li, J. & Wang, T. Recent advances in application of alkoxy radical in organic synthesis. *Organics* **4**, 459–489 (2023).
13. Li, P. et al. Modulating electron transfer via cerium photocatalysis for alkoxy radical-mediated selective hydroetherification. *Angew. Chem. Int. Ed.* **64**, e202501949 (2025).
14. Mao, R. et al. Biocatalytic, enantioenriched primary amination of tertiary C–H bonds. *Nat. Catal.* **7**, 585–592 (2024).
15. Emmanuel, M. A., Greenberg, N. R., Oblinsky, D. G. & Hyster, T. K. Accessing non-natural reactivity by irradiating nicotinamide-dependent enzymes with light. *Nature* **540**, 414–417 (2016).
16. Peng, Y. et al. Photoinduced promiscuity of cyclohexanone monooxygenase for the enantioselective synthesis of α-fluoroketones. *Angew. Chem. Int. Ed.* **61**, e202211199 (2022).
17. Zhou, Q., Chin, M., Fu, Y., Liu, P. & Yang, Y. Stereodivergent atom-transfer radical cyclization by engineered cytochromes P450. *Science* **374**, 1612–1616 (2021).
18. Rui, J. et al. Directed evolution of nonheme iron enzymes to access abiological radical-relay C(sp^3)–H azidation. *Science* **376**, 869–874 (2022).
19. Jain, S., Ospina, F. & Hammer, S. C. A new age of biocatalysis enabled by generic activation modes. *JACS Au* **4**, 2068–2080 (2024).
20. Toogood, H. S. & Scrutton, N. S. Discovery, characterization, engineering, and applications of ene-reductases for industrial biocatalysis. *ACS Catal.* **8**, 3532–3549 (2018).
21. Baker Dockrey, S. A. & Narayan, A. R. H. Flavin-dependent biocatalysts in synthesis. *Tetrahedron* **75**, 1115–1121 (2019).
22. Kumar Roy, T., Sreedharan, R., Ghosh, P., Gandhi, T. & Maiti, D. Ene-reductase: a multifaceted biocatalyst in organic synthesis. *Chem. Eur. J.* **28**, e202103949 (2022).
23. Stephenson, C. R. J., Yoon, T. P. & MacMillan, D. W. C. *Visible Light Photocatalysis in Organic Chemistry* (Wiley, 2018).
24. Mondal, S. et al. Enantioselective radical reactions using chiral catalysts. *Chem. Rev.* **122**, 5842–5976 (2022).
25. Harrison, W., Huang, X. & Zhao, H. Photobiocatalysis for abiological transformations. *Acc. Chem. Res.* **55**, 1087–1096 (2022).
26. Fu, H. & Hyster, T. K. From ground-state to excited-state activation modes: flavin-dependent "ene"-reductases catalyzed non-natural radical reactions. *Acc. Chem. Res.* **57**, 1446–1457 (2024).
27. Biegasiewicz, K. F. et al. Photoexcitation of flavoenzymes enables a stereoselective radical cyclization. *Science* **364**, 1166–1169 (2019).
28. Liu, Y. et al. Asymmetric synthesis of α-chloroamides via photoenzymatic hydroalkylation of olefins. *J. Am. Chem. Soc.* **146**, 7191–7197 (2024).
29. Huang, X. et al. Photoenzymatic enantioselective intermolecular radical hydroalkylation. *Nature* **584**, 69–74 (2020).
30. Li, M., Harrison, W., Zhang, Z., Yuan, Y. & Zhao, H. Remote stereocontrol with azaarenes via enzymatic hydrogen atom transfer. *Nat. Chem.* **16**, 277–284 (2024).
31. Duan, X. et al. A photoenzymatic strategy for radical-mediated stereoselective hydroalkylation with diazo compounds. *Angew. Chem. Int. Ed.* **62**, e202214135 (2023).
32. Zhu, C. et al. Photoenzymatic enantioselective synthesis of oxygen-containing benzo-fused heterocycles. *Angew. Chem. Int. Ed.* **62**, e202311762 (2023).
33. Crisenza, G. E. M., Mazzarella, D. & Melchiorre, P. Synthetic methods driven by the photoactivity of electron donor–acceptor complexes. *J. Am. Chem. Soc.* **142**, 5461–5476 (2020).
34. Zhao, B. et al. Direct visible-light-excited flavoproteins for redox-neutral asymmetric radical hydroarylation. *Nat. Catal.* **6**, 996–1004 (2023).
35. Yu, J. et al. Repurposing visible-light-excited ene-reductases for diastereo- and enantioselective lactones synthesis. *Angew. Chem. Int. Ed.* **63**, e202402673 (2024).
36. Ye, Y. et al. Using enzymes to tame nitrogen-centred radicals for enantioselective hydroamination. *Nat. Chem.* **15**, 206–212 (2023).
37. Zhang, Z. et al. Photoenzymatic enantioselective intermolecular radical hydroamination. *Nat. Catal.* **6**, 687–694 (2023).
38. Harrison, W. et al. Photoenzymatic asymmetric hydroamination for chiral alkyl amine synthesis. *J. Am. Chem. Soc.* **146**, 10716–10722 (2024).
39. Shi, F. et al. Enantioselective biosynthesis of vicinal diamines enabled by synergistic photo/biocatalysis consisting of an ene-reductase and a green-light-excited organic dye. *Chin. J. Catal.* **68**, 223–229 (2025).
40. Chen, X. et al. Photoenzymatic hydrosulfonylation for the stereoselective synthesis of chiral sulfones. *Angew. Chem. Int. Ed.* **62**, e202218140 (2023).
41. Jiang, L. et al. Photoenzymatic redox-neutral radical hydrosulfonylation initiated by FMN. *ACS Catal.* **14**, 6710–6716 (2024).
42. Shi, Q. et al. Single-electron oxidation-initiated enantioselective hydrosulfonylation of olefins enabled by photoenzymatic catalysis. *J. Am. Chem. Soc.* **146**, 2748–2756 (2024).
43. Xu, Y. et al. A light-driven enzymatic enantioselective radical acylation. *Nature* **625**, 74–78 (2024).
44. Chen, B. et al. Modular access to chiral amines via imine reductase-based photoenzymatic catalysis. *J. Am. Chem. Soc.* **146**, 14278–14286 (2024).
45. Zhang, J. et al. Photoenzymatic conversion of enamides to enantioenriched benzylic amines enabled by visible-light-induced single-electron reduction. *ACS Catal.* **13**, 15682–15690 (2023).
46. Gould, I. R., Shukla, D., Giesen, D. & Farid, S. Energetics of electron-transfer reactions of photoinitiated polymerization: dye-sensitized fragmentation of *N*-alkoxypyridinium salts. *Helv. Chim. Acta* **84**, 2796–2812 (2001).

47. Stewart, R. C. & Massey, V. Potentiometric studies of native and flavin-substituted old yellow enzyme. *J. Biol. Chem.* **260**, 13639–13647 (1985).
48. Sandoval, B. A., Meichan, A. J. & Hyster, T. K. Enantioselective hydrogen atom transfer: discovery of catalytic promiscuity in flavin-dependent 'ene'-reductases. *J. Am. Chem. Soc.* **139**, 11313–11316 (2017).
49. Duan, X. et al. Ground-state flavin-dependent enzymes catalyzed enantioselective radical trifluoromethylation. *Nat. Commun.* **16**, 1225 (2025).
50. Xu, J. et al. Stereodivergent protein engineering of a lipase to access all possible stereoisomers of chiral esters with two stereocenters. *J. Am. Chem. Soc.* **141**, 7934–7945 (2019).
51. Bao, Y., Xu, Y. & Huang, X. Focused rational iterative site-specific mutagenesis (FRISM): a powerful method for enzyme engineering. *Mol. Catal.* **553**, 113755 (2024).
52. Jumper, J. et al. Highly accurate protein structure prediction with AlphaFold. *Nature* **596**, 583–589 (2021).
53. Trott, O. & Olson, A. J. AutoDock Vina: improving the speed and accuracy of docking with a new scoring function, efficient optimization, and multithreading. *J. Comput. Chem.* **31**, 455–461 (2010).
54. Maier, J. A. et al. ff14SB: improving the accuracy of protein side chain and backbone parameters from ff99SB. *J. Chem. Theory Comput.* **11**, 3696–3713 (2015).
55. Wang, J., Wolf, R. M., Caldwell, J. W., Kollman, P. A. & Case, D. A. Development and testing of a general amber force field. *J. Comput. Chem.* **25**, 1157–1174 (2004).
56. Becke, A. D. Density-functional thermochemistry. III. The role of exact exchange. *J. Chem. Phys.* **98**, 5648–5652 (1993).
57. Jorgensen, W. L., Chandrasekhar, J., Madura, J. D., Impey, R. W. & Klein, M. L. Comparison of simple potential functions for simulating liquid water. *J. Chem. Phys.* **79**, 926–935 (1983).
58. Case, D. A. et al. *AMBER 2018* (Univ. of California, 2018).
59. Metz, S., Kästner, J., Sokol, A. A., Keal, T. W. & Sherwood, P. ChemShell—a modular software package for QM/MM simulations. *WIREs Comput. Mol. Sci.* **4**, 101–110 (2014).
60. Lu, Y. et al. Multiscale QM/MM modelling of catalytic systems with ChemShell. *Phys. Chem. Chem. Phys.* **25**, 21816–21835 (2023).
61. Furche, F. et al. Turbomole. *WIREs Comput. Mol. Sci.* **4**, 91–100 (2014).
62. Smith, W. & Forester, T. R. DL_POLY_2.0: a general-purpose parallel molecular dynamics simulation package. *J. Mol. Graph.* **14**, 136–141 (1996).
63. Smith, W., Yong, C. W. & Rodger, P. M. DL_POLY: application to molecular simulation. *Mol. Simul.* **28**, 385–471 (2002).
64. Bakowies, D. & Thiel, W. Hybrid models for combined quantum mechanical and molecular mechanical approaches. *J. Phys. Chem.* **100**, 10580–10594 (1996).
65. Grimme, S. Semiempirical GGA-type density functional constructed with a long-range dispersion correction. *J. Comput. Chem.* **27**, 1787–1799 (2006).
66. Grimme, S., Ehrlich, S. & Goerigk, L. Effect of the damping function in dispersion corrected density functional theory. *J. Comput. Chem.* **32**, 1456–1465 (2011).
67. Zhang, Q. Steering oxygen-centred radicals with ground-state ene-reductases for enantioselective intermolecular hydroalkoxylations. *Zenodo* https://doi.org/10.5281/zenodo.14851048 (2025).

Acknowledgements

This work was supported by the National Key Research and Development Program of China (grant number 2022YFA0913000 to X.H.), the National Natural Science Foundation of China (grant numbers 22277053 to X.H., 22121001 to B.W. and 224B2705 to B.Z.), the Fundamental Research Funds for the Central Universities (grant numbers 0205/14380346 and 0205/14380351 to X.H.) and the Excellent Research Program of Nanjing University (grant number ZYJH004), the State Key Laboratory of Microbial Technology Open Projects Fund (M2023-01 to B.W.).

Author contributions

B.C. envisioned and developed the reaction. B.Z. assisted with synthetic experiments. J.Y. and R.G. created mutations and expressed proteins. Q.Z., D.L. and B.W. conducted computational studies. Z.Z. reproduced selected examples. B.C., Q.Z., B.W. and X.H. wrote the paper with input from all authors. X.H. coordinated and conceived the project.

Competing interests

The authors declare no competing interests.

Additional information

Supplementary information The online version contains supplementary material available at https://doi.org/10.1038/s41929-025-01372-z.

Correspondence and requests for materials should be addressed to Binju Wang or Xiaoqiang Huang.

Peer review information *Nature Catalysis* thanks Maciej Szaleniec and the other, anonymous, reviewer(s) for their contribution to the peer review of this work.

nature portfolio

Corresponding author(s): Binju Wang, Xiaoqiang Huang

Last updated by author(s): May 19, 2025

Reporting Summary

Nature Portfolio wishes to improve the reproducibility of the work that we publish. This form provides structure for consistency and transparency in reporting. For further information on Nature Portfolio policies, see our Editorial Policies and the Editorial Policy Checklist.

Statistics

For all statistical analyses, confirm that the following items are present in the figure legend, table legend, main text, or Methods section.

n/a	Confirmed
☐	☒ The exact sample size (*n*) for each experimental group/condition, given as a discrete number and unit of measurement
☐	☒ A statement on whether measurements were taken from distinct samples or whether the same sample was measured repeatedly
☒	☐ The statistical test(s) used AND whether they are one- or two-sided *Only common tests should be described solely by name; describe more complex techniques in the Methods section.*
☒	☐ A description of all covariates tested
☒	☐ A description of any assumptions or corrections, such as tests of normality and adjustment for multiple comparisons
☐	☒ A full description of the statistical parameters including central tendency (e.g. means) or other basic estimates (e.g. regression coefficient) AND variation (e.g. standard deviation) or associated estimates of uncertainty (e.g. confidence intervals)
☒	☐ For null hypothesis testing, the test statistic (e.g. *F*, *t*, *r*) with confidence intervals, effect sizes, degrees of freedom and *P* value noted *Give P values as exact values whenever suitable.*
☒	☐ For Bayesian analysis, information on the choice of priors and Markov chain Monte Carlo settings
☒	☐ For hierarchical and complex designs, identification of the appropriate level for tests and full reporting of outcomes
☒	☐ Estimates of effect sizes (e.g. Cohen's *d*, Pearson's *r*), indicating how they were calculated

Our web collection on statistics for biologists contains articles on many of the points above.

Software and code

Policy information about availability of computer code

Data collection	All catalytic reactions were performed in a clear glass vial (4 mL or 250 mL) with magnetic stirring, and stirred for 12/24 h. Reagents were purchased from Adamas-beta, Energey Chemical and Bide Pharmatech Ltd., respectively, and used without further purification. Flash column chromatography was performed with ultrapure silica gel SiliaFlash® P60 (irregularly shaped, 200-300 mesh). 1H NMR and 13C NMR spectra were recorded on a BRUKER AVANCE III 400 MHz NMR spectrometer at ambient temperature. NMR standards were used as follows: 1H NMR spectroscopy: δ = 0.00 ppm (TMS); 13C NMR spectroscopy: δ = 77.0 ppm (CDCl3), δ = 36.5 ppm (DMSO-d6). 1H NMR coupling constants were reported in Hz, and multiplicity was indicated as follows: s (singlet); d (doublet); t (triplet); quint (quintet); sext (sextet); m (multiplet); dd (doublet of doublets); dt (doublet of triplets). High-resolution mass spectra (HRMS) were conducted at Thermo Fisher Micromass instrument with an electrospray ionization time-of-flight (ESI-TOF) detector. The GC-MS system consisted of an Agilent 8860 (Agilent Inc, Palo Alto, CA, USA) gas chromatograph (unless noted DB-5MS UI column was used, length 30 m, inner diameter 0.25 mm, film thickness 0.25 µm), and an Agilent 5977B mass selective detector (positive electron impact mode, EI). An Agilent 8860 gas chromatograph (HP-5 column, length 30 m, inner diameter 0.32 mm, film thickness 0.25 µm) with an FID detector was used for yield determination. Analytical high performance liquid chromatography (HPLC) was carried out using an Agilent 1290 Infinity II LC System and yields were determined on a Poroshell EC-C18 column (4.6 x 150 mm, 4 µm) against an internal standard 1,3,5-tribromobenzene (TBB) at 210 nm. Enantioselectivity of the reaction products were determined with a 25 cm Daicel Chiralcel OD-3 column, a 25 cm Daicel Chiralcel OJ-3 column, a 25 cm Daicel Chiralpak AS-H column or a 25 cm Daicel Chiralcel OJ-H column on an Agilent 1260 Infinity II system or Waters e2695 system using hexanes/isopropanol as the mobile phase. The AutoDock version used is v4.2.6.
Data analysis	Yield determined by GC was relative to the n-dodecane internal standard according to a calibration curve. Yield determined by LC was relative to the 1,3,5-tribromobenzene internal standard according to a calibration curve. Enantioselectivity was determined by chiral HPLC.

For manuscripts utilizing custom algorithms or software that are central to the research but not yet described in published literature, software must be made available to editors and reviewers. We strongly encourage code deposition in a community repository (e.g. GitHub). See the Nature Portfolio guidelines for submitting code & software for further information.

Data

Policy information about availability of data

All manuscripts must include a data availability statement. This statement should provide the following information, where applicable:

- Accession codes, unique identifiers, or web links for publicly available datasets
- A description of any restrictions on data availability
- For clinical datasets or third party data, please ensure that the statement adheres to our policy

High-performance liquid chromatography spectra and NMR spectra are available in the Supplementary Information. The PDB code of the GluER used in this work is 6O08. The structural data (including all QM calculation coordinates and QM region coordinates from QM/MM calculations) is available in Zenodo at https://doi.org/10.5281/zenodo.14851048. The files and codes for building the QSAR model are available at https://github.com/ld139/QSAR_enz.

Research involving human participants, their data, or biological material

Policy information about studies with human participants or human data. See also policy information about sex, gender (identity/presentation), and sexual orientation and race, ethnicity and racism.

Reporting on sex and gender	not applicable
Reporting on race, ethnicity, or other socially relevant groupings	not applicable
Population characteristics	not applicable
Recruitment	not applicable
Ethics oversight	not applicable

Note that full information on the approval of the study protocol must also be provided in the manuscript.

Field-specific reporting

Please select the one below that is the best fit for your research. If you are not sure, read the appropriate sections before making your selection.

☒ Life sciences ☐ Behavioural & social sciences ☐ Ecological, evolutionary & environmental sciences

For a reference copy of the document with all sections, see nature.com/documents/nr-reporting-summary-flat.pdf

Life sciences study design

All studies must disclose on these points even when the disclosure is negative.

Sample size	Scope investigation was conduct in 0.008 mmol reactions as the amount of the products formed is enough for yields determined by GC. Substrates (3a and 3g) were selected to performed in 0.1 mmol scale to obtain isolated yields as 0.1 mmol scale typically gives ~10 mg isolated products.
Data exclusions	No data were excluded.
Replication	All enzymatic reactions were repeated at least twice. All attempts at replication were successful.
Randomization	not applicable. No group allocation involved in this study.
Blinding	not applicable. No group allocation involved in this study.

Reporting for specific materials, systems and methods

We require information from authors about some types of materials, experimental systems and methods used in many studies. Here, indicate whether each material, system or method listed is relevant to your study. If you are not sure if a list item applies to your research, read the appropriate section before selecting a response.

Materials & experimental systems

n/a	Involved in the study
☒	☐ Antibodies
☒	☐ Eukaryotic cell lines
☒	☐ Palaeontology and archaeology
☒	☐ Animals and other organisms
☒	☐ Clinical data
☒	☐ Dual use research of concern
☒	☐ Plants

Methods

n/a	Involved in the study
☒	☐ ChIP-seq
☒	☐ Flow cytometry
☒	☐ MRI-based neuroimaging

Plants

Seed stocks	not applicable
Novel plant genotypes	not applicable
Authentication	not applicable